SYNCHROTRON EMISSION FROM THE SHELL-LIKE SUPERNOVA REMNANTS AND THE COSMIC-RAY ORIGIN

Hiroshi TOMIDA

Department of Physics. Graduated School of Science,
Kyoto University, Sakyo-ku, Kyoto 606-8502, Japan

Submitted to the Department of Physics,
Kyoto University on January 5, 1999,
in partial fulfillment of the requirements for
the degree of Doctor of Philosophy

Abstract

We observed three shell-like supernova remnants (SNRs; G347.3–0.5, RCW86, and G156.2+5.7) with the ASCA satellite. With the spectroscopic and imaging analysis, we found both non-thermal and thermal X-rays from all of these SNRs.

The thermal emission of G347.3–0.5 is weak. This indicates that the SNR is either old, or very young with small swept-up matter. In RCW86, we found that the abundance pattern for each element is similar to that of SNR 0102-72.3 in the Small Magellanic Cloud. This suggests that RCW86 has type-II SN origin, and is consistent with the report that RCW86 resides in an OB star association. In G156.2+5.7, we found abundance concentration in the SNR center region. This is the second example among the middle-aged SNRs after Cygnus Loop. We suspect that some amount of ejecta still remains in the core region.

The non-thermal component is likely to be synchrotron emissions from extremely high-energy electrons. These discoveries of the synchrotron X-rays in shell-like SNRs follows those of SN1006, CasA, and IC443. Comparing the X-ray data with the radio results, we found that the synchrotron spectra break at $5 - 400$eV. This indicates that the electron spectra break at (5–40)$\times 10^{12}$eV, which are higher than the break energy of the electron spectrum observed at the earth. The electron spectra are well described with the standard acceleration model. Neither SN-type nor direction of the magnetic field is essential for the acceleration efficiency. Using the model, we estimated the possible maximum energy of protons to be $\sim 10^{14.5}$eV, which is close to so called 'knee' energy. We also estimated the total energy of electrons accelerated in SNRs to be $\sim 2\times 10^{47}$erg in average. We may approach to a goal to solve the long-standing problem of acceleration mechanism of the cosmic-ray, at least to energies less than $10^{14.5}$ eV.

Contents

1 Introduction **10**

2 Review **12**

2.1 Supernova and Supernova Remnant 12

2.1.1 Type-Ia and Type-II Explosion 12

2.1.2 Shock Wave 14

2.1.3 Evolution of Supernova Remnant 15

2.1.4 Plasma Condition 17

2.2 Shell-like Supernova Remnants and Crab-like Pulsar 19

2.2.1 Shell-like SNR 19

2.2.2 Crab-like pulsar 19

2.3 Cosmic Ray 20

2.3.1 Energy Spectrum 20

2.3.2 Chemical Composition 22

2.3.3 Energy Budget 22

2.3.4 Acceleration of Cosmic Rays 24

2.3.5 Observational Evidence for Comic-Ray Acceleration in SNRs 25

2.4 X-ray Emission from Supernova Remnants 28

2.4.1 Bremsstrahlung (Free–Free Emission) 28

2.4.2 Line Emission (Bound-Bound Emission) 28

2.4.3 Synchrotron Emission 29

2.4.4 Inverse Compton 30

3 Instruments **32**

3.1 ASCA 32

3.2 XRT 32

3.3 GIS . . . 36
  3.3.1 Overview . . . 36
  3.3.2 Background Rejection . . . 38
  3.3.3 Observation Mode . . . 38
  3.3.4 Response Function . . . 39
  3.3.5 Data Screening . . . 40
3.4 SIS . . . 41
  3.4.1 Overview . . . 41
  3.4.2 CCD . . . 41
  3.4.3 SIS Configuration . . . 42
  3.4.4 Event Extraction . . . 46
  3.4.5 SIS DE . . . 46
  3.4.6 Data Screening . . . 48
3.5 ROSAT . . . 51

4 G347.3–0.5 (RX J1713.7-3946) 52
4.1 Review . . . 52
4.2 Observation . . . 52
4.3 Image Analysis . . . 55
4.4 Spectrum Analysis . . . 56
  4.4.1 Bright Rims and the Rest Region . . . 56
  4.4.2 Point Sources . . . 69
4.5 Discussion for G347.3-0.5 . . . 69
  4.5.1 Hard X-ray component . . . 69
  4.5.2 Distance to G347.3–0.5 . . . 71
  4.5.3 Thermal Emission . . . 72
  4.5.4 Shell Structure . . . 72
  4.5.5 Point Sources . . . 73

5 RCW86(G315.4-2.3) 75
5.1 Review . . . 75
5.2 Observation and Data Screening . . . 76
5.3 Image Analysis and the Results . . . 76
5.4 Spectrum Analysis and Results . . . 78

5.4.1 SW(southwest)-1 Region 81

5.4.2 SW(southwest)-2 Region 83

5.4.3 Northeast Shell 88

5.4.4 East Shell 89

5.4.5 North Shell 90

5.4.6 Inner Region 92

5.4.7 Hard Spot 94

5.4.8 Fe k α Line 95

5.5 Discussion for RCW86 95

5.5.1 Two Component Model 95

5.5.2 6.4keV Line 99

5.5.3 Distance 100

5.5.4 Sedov Solution 101

6 G156.2+5.7(RX J04591+5147) 102

6.1 Review 102

6.2 Observation and Data Screening 102

6.3 Analysis and Results 103

6.3.1 Image Analysis 103

6.3.2 Spectrum Analysis 106

6.4 Discussion for G156.2+5.7 111

6.4.1 NEI Plasma in G156.2+5.7 111

6.4.2 The Hard X-ray Tail of G156.2+5.7 115

6.4.3 AX J0050+5238 117

7 Discussion on the Acceleration of Cosmic Rays 118

7.1 Wide Band Spectrum 118

7.1.1 Spectra of Cosmic Electrons in SNRs 120

7.2 Energy Budget of Cosmic Rays 120

7.3 Acceleration Model 122

7.3.1 Comparison with an Acceleration Model 122

7.3.2 Break Energy of the Proton Spectrum 123

7.4 Comparison with Other Results 125

7.5 Direction of the Magnetic Field 126

7.6 SN–type 127
7.7 Other Candidates for the Cosmic-ray Source 128

8 Conclusion **129**

A Diffusive Acceleration Model **131**

List of Figures

2.1 Schematic view around the shock front 13
2.2 Cooling function 18
2.3 Example of shell-like SNRs 20
2.4 Energy spectrum of cosmic protons 21
2.5 Chemical composition of cosmic-ray 22
2.6 Energy spectrum of cosmic electrons 23
2.7 A schematic view of the Fermi acceleration 25
2.8 ASCA/GIS image of SN1006 26
2.9 ASCA/SIS spectrum of SN1006 27
2.10 Profile of $F(x)$ 30

3.1 Schematic view of ASCA 33
3.2 Rough sketch of XRT 33
3.3 Effective area of XRT (1) 34
3.4 Effective area of XRT (2) 34
3.5 The point spread function of ASCA XRT 35
3.6 The stray light of ASCA XRT 35
3.7 The cross section view of GIS 36
3.8 The schematic view of GIS 37
3.9 The effective area of XRT+GIS 40
3.10 Schematic view of CCD 42
3.11 Cross section of CCD 43
3.12 Charge transfer in CCD 43
3.13 SIS chip configuration 44
3.14 The detection efficiency of SIS 44
3.15 The cross section of SIS camera body 45
3.16 Signal block diagram of SIS 45

3.17 SIS grade definition 47

4.1 G347.3-0.5 GIS image with FOV of ASCA 54
4.2 G347.3-0.5 GIS image 57
4.3 G347.3-0.5 ROSAT image 58
4.4 G347.3-0.5 radio image with GIS contours 59
4.5 GIS image around the source E in G347.3–0.5 59
4.6 Regions from which spectra were extracted 61
4.7 The background subtracted G347.3-0.5 GIS spectra of the four bright rims and diffuse component 62
4.8 The summed-up spectrum from G347.3–0.5 rims and diffuse regions 63
4.9 The summed-up SIS spectrum of G347.3–0.5 66
4.10 G347.3–0.5 SIS spectrum with one component model 66
4.11 The galactic X-ray ridge emission near G347.3–0.5 67
4.12 G347.3–0.5 SIS spectrum with two component model 68
4.13 GIS/SIS spectrum of source W in G347.3–0.5 70
4.14 The power spectrum of the source W in G347.3–0.5 70
4.15 ROSAT/PSPC spectrum of source W and E in G347.3–0.5 71
4.16 CANGAROO image of G347.3–0.5 72
4.17 A simulated image of uniform density sphere and shell 74

5.1 RCW86 *ROSAT*-PSPC image and the F.O.V of ASCA 77
5.2 RCW86 mosaic image 79
5.3 RCW86 SIS image around the SW shell 80
5.4 RCW86 radio image 80
5.5 *ROSAT*-PSPC image around the hard spot 81
5.6 RCW86 GIS image with separated regions 82
5.7 SIS spectrum of SW-1 region of RCW86 (1) 84
5.8 SIS spectrum of SW-1 region of RCW86 (2) 84
5.9 GIS spectrum of SW-1 region of RCW86 (1) 85
5.10 SIS spectrum of SW-1 region of RCW86 (3) 85
5.11 GIS spectrum of SW-1 region of RCW86 (2) 86
5.12 Spectrum from SW2 shell of RCW86 87
5.13 RCW86 X-ray of the north east region 89
5.14 RCW86 spectrum of the east shell 91

5.15 RCW86 X-ray spectrum of the north shell 92
5.16 RCW86 X-ray spectrum of the inner region 93
5.17 Spectrum of RCW86 hard spot 94
5.18 Power spectrum of RCW86 hard spot 95
5.19 RCW86 Fe k line image 96
5.20 RCW86 Fe k line spectra 96
5.21 Schematic vie of 6.4 keV source 100

6.1 G156.2+5.7 ROSAT/PSPC mosaic image 104
6.2 G156.2+5.7 GIS image 105
6.3 *ROSAT*/PSPC image of AX J0500+5238 106
6.4 G156.2+5.7 SIS spectrum 108
6.5 G156.2+5.7 GIS spectrum 109
6.6 G156.2+5.7 GIS spectrum 109
6.7 AX J0500+5238 GIS spectrum 111
6.8 Power-spectrum of AX J0050+5238 112
6.9 The narrow band image of G156.2+5.7 obtained with GIS in 1.6–2.0 keV (Si band)114
6.10 The narrow band image of G156.2+5.7 in 1.6–2.0 keV (Si band) 114
6.11 SIS spectrum from the center region of G156.2+5.7 115

7.1 Synchrotron spectrum from radio to X-ray 119
7.2 A theoretical model of the maximum energy for electrons accelerated by diffusive (Fermi) model 124
7.3 A theoretical model of the maximum energy for protons accelerated by diffusive (Fermi) model 125
7.4 SNR structures 127

A.1 time dependence of the maximum energy 133

List of Tables

2.1 The energy density of various elements 21

3.1 GIS temporal resolution 39

3.2 SIS temporal resolution 49

4.1 G347.3–0.5 attitude parameters 53

4.2 The GIS bit assignment for telemetry data 53

4.3 Observation time of G347.3–0.5 53

4.4 G347.3 fitting results for the spectra from the four rims and the rest region . . . 60

4.5 X-ray flux of G347.3–0.5 in five regions 61

4.6 The fitting results of the summed-up spectra (GIS) 61

4.7 Model parameters of Galactic plane background near G347.3–0.5 65

4.8 The fitting results of G347.3-0.5(SIS : one component) 65

4.9 Regions we used for the galactic diffuse emission. 67

4.10 The fitting results of the SIS spectrum of GRXE 68

4.11 The spectrum fit results G347.3-0.5(SIS : two components) 68

4.12 The results for the sources W in G347.3-0.5 69

4.13 N_H and the distance of the galactic SNRs near the galactic plane 73

5.1 Observation parameters (attitude) of RCW86 76

5.2 Observation time of RCW86 76

5.3 Fitting results of the SW1 region 86

5.4 The fitting results for SW2 region of RCW86 88

5.5 Fitting results of the north east shell 89

5.6 Fitting results of the east shell 91

5.7 Fitting results of the north shell 91

5.8 The fitting results for the inner region of RCW86 93

5.9 Fitting results of the hard spot 94

5.10 6.4kev line in RCW86 97
5.11 The best models of RCW86 97

6.1 G156.2+5.7 attitude parameters 103
6.2 G156.2+5.7 observation time 103
6.3 Spectral fitting results of G156.2+5.7 110
6.4 Spectral fitting result of AX J0050+5238 112

7.1 Synchrotron break energy 119
7.2 Total energy of accelerated electrons in the SNRs 122

Chapter 1

Introduction

Supernova remnant (SNR) is one of the most frequently observed objects in X-ray astronomy. Many workers have studied its abundance of heavy elements, temperature, ionization degree, and so on. They are all concerned with the thermal plasma heated by the blast wave shock. Studies on the non-thermal emission are mostly related with pulsars

Cosmic rays, which were discovered about 90 years ago (Hess 1911, 1912), have an energy density higher than that of the magnetic field, radiation field, and so on. Therefore they comprise a major constituent of the interstellar medium. One of the most interesting and unresolved subjects on the cosmic rays is its energy origin and the acceleration mechanism. The energy spectrum of cosmic rays is represented by a power-law function with a break called 'knee' at $10^{15.5}$eV. It has been thought that the origin of cosmic rays below the knee energy might be in the galaxy, although little evidence has been found. The most plausible and generally accepted model, at least for the low energy part, is the (first order) Fermi process in SNR shock fronts. Thus SNR would be a key object which may be closely related to the galactic cosmic-ray origin.

Since charged particles are scattered by the magnetic field in the interstellar space, we cannot identify the position (direction) of cosmic ray sources with the direct detection of cosmic-rays .

On the other hand, electromagnetic wave travels straight in the magnetic field. If SNRs are the birth place of cosmic rays, its density would be very high in SNRs. We can expect radiation due to synchrotron, inverse Compton scattering, bremsstrahlung, nuclear reaction, and so on. Thus electromagnetic waves can be very powerful to investigate cosmic rays, particularly to identify the source positions.

In recent years, X-ray and gamma ray observations brought a breakthrough on the particle acceleration in SNRs. Koyama *et al* (1995) reported on the non-thermal X-rays from SN1006.

The shell-like structure and the good coincidence of the X-ray image with the radio one indicated the synchrotron emission from ∼100 TeV electrons, which is close to the knee energy. Gamma-rays due to inverse Compton scatterings have confirmed the existence of high energy electrons in SNRs (Tanimori *et al* 1998) .

Since the Fermi mechanism has no difference on the acceleration efficiency between electrons and protons, and protons are the main composition of cosmic rays , these discoveries have been recognized as strong evidence for the Fermi acceleration in SNRs. Gamma-rays form due to π^0 decays also gave more direct evidence for the cosmic ray acceleration in SNRs (Esposite 1996).

Although, key information for the cosmic ray origin is gradually accumulating from the various wave-length, quantitative studies are still insufficient.

This paper, consequently, is intended to study on the next subjects;

(1) find further samples of non-thermal emission from shell-like SNRs, and make quantitative studies on cosmic rays,
(2) investigate whether SNRs are the primary origin of cosmic rays,
(3) provide some constraints on the acceleration theory.

As for SNR X-rays, thermal component including line emission is prevailing in the soft energy band, while the non-thermal component extends to the hard X-ray band. Thus good energy resolution to resolve the line structure and the wide energy band are essential for the study of the non-thermal emission from SNRs. Since origin (cite) of thermal and non-thermal X-rays are not identical, imaging capability is also required

The ASCA satellite, developed under a Japan-US collaboration, was successfully launched in 1993 (Tanaka *et al* 1994). This is the fourth Japanese satellite for X-ray astronomy after Hakucho, Temma, and Ginga. ASCA is the first satellite to exhibit a wide band imaging and spectroscopic capability, hence has brought us the many remarkable results on the high energy universe. ASCA is the ideal observatory at present for our study, as is demonstrated by the observation of SN1006.

We observed three shell-like SNRs, G347.3–0.5, RCW86, and G156.2+5.7, with ASCA. In the following sections, we study the non-thermal emission from the shell-like SNRs. In chapter 2, a review of SNRs and cosmic rays are presented. The ASCA satellite and its main instruments are explained in chapter 3. In chapter 4–6, the analysis, results, and the brief summary of the ASCA observations are presented. In chapter 7, we make the discussion on cosmic-ray origin. Finally we summarize our study.

Chapter 2

Review

2.1 Supernova and Supernova Remnant

Supernova (SN) is an explosive event which occurs at the end of star's life. There are two types of supernovae; type-I and type-II (section 2.1.1). Type-I SNe exhibit the hydrogen lines in their spectra, while type-II SNe do not. Presence (absence) of the hydrogen lines indicates that there are (not) hydrogen envelope around the progenitor star before the explosion. After the explosion, the huge explosion energy affects the surrounding matter. For example, the circumstellar and interstellar medium are heated by the shock wave (section 2.1.2), which are observed as supernova remnants (SNRs). SNRs evolve with time (section 2.1.3). The heated matter can be treated as high temperature plasma (section 2.1.4). In this section, we will briefly review SN and SNR.

2.1.1 Type-Ia and Type-II Explosion

Type-Ia Supernova

Classical Type-I SN is currently recognized as Type-Ia SN. The 'standard' model of Type-Ia explosion is described as following (Nomoto *et al* 1984). There is a closed binary system consisting of a white dwarf (WD) and a companion star. The WD consists of carbon and oxygen. In the case that the rate of the mass transfer ($\dot{M}$) from the companion star into the WD through Roche-lobe overflow is larger than 3×10^{-6} $M_\odot$ year^{-1} ($M_\odot$ is the solar mass), the accreting matter escapes from the WD since the temperature becomes too high. In the case that the transfer rate is smaller than 1×10^{-8} $M_\odot$ year^{-1}, the accreting matter also escapes from the WD due to small explosions at the surface of the WD. Accordingly, the accretion

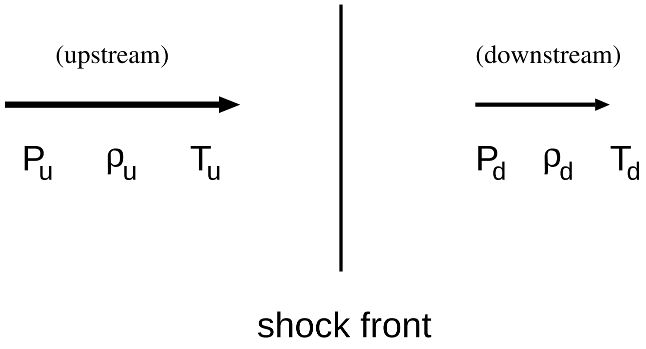

Figure 2.1: A schematic view around the shock front. Subscripts 'u' and 'd' denote upstream and downstream, respectively

matter can be accumulated in the case of $1 \times 10^{-8} < \dot{M} < 3 \times 10^{-6} M_{\odot}$ year^{-1}. When the total mass of the WD exceeds the Chandrasekhar limit (~1.4 $M_{\odot}$), explosive ignition occurs in the electron-degenerated matter, which makes a carbon deflagration. The ignition and the deflagration produce the heavy elements such as Fe, Ni, Ca, Ar, S, Si, and so on. The total explosion energy is estimated to be 1.3×10^{51} erg, and the ejected mass is about 1.4 $M_{\odot}$.

Type-II Supernova

Type-II SN is explained by the gravitational collapse of stars. At the end of the evolution of a massive star ($M > 8 M_{\odot}$), the iron core is formed at the center, which is supported by the degeneracy pressure of electrons. When the temperature exceeds $10^{10} K$, electron-capture reactions and endothermic decompositions of Fe occur, hence the number of electrons is reduced, and the pressure becomes low. Accordingly, the gravitational collapse starts, since the core cannot support itself. When the central density exceeds 2.7×10^{14} g cm^{-3} due to the collapsing matter, the central core can support itself. At the surface of the core, the further collapsing matter is bounced back into the outer direction, which forms a shock wave. If the shock has enough energy, the further collapsing matter is blown back with kinetic energy of ~10^{51}erg. This is type-II SN. The central core becomes a neutron star (or a black-hole). Type-II supernovae are not observed in early type galaxies, which consist of old type stars and little cold gas. These indicate that the progenitors of Type-II SN are early type stars.

2.1.2 Shock Wave

In this subsection, we briefly review the shock wave. Figure 2.1 is a schematic view around a shock front. In a coordinate moving with the shock front, the conservation of mass, energy, and momentum are described as

$$\frac{\partial \rho}{\partial t} + \frac{\partial(\rho v)}{\partial x} = 0 \tag{2.1}$$

$$\frac{\partial(\rho v)}{\partial t} + \frac{\partial(\rho v^2 + P)}{\partial x} = 0 \tag{2.2}$$

$$\frac{\partial}{\partial t}\{\rho(\frac{1}{2}v^2 + E)\} + \frac{\partial}{\partial x}\{Pv + \rho(\frac{1}{2}v^2 + E)v\} = 0 \tag{2.3}$$

where ρ, v, P, and E are density, velocity, pressure, and energy per unit mass, respectively. Applying these equations to the situation shown in figure 2.1, we obtain

$$\rho_u v_u = \rho_d v_d \tag{2.4}$$

$$\rho_u v_u^2 + P_u = \rho_d v_d^2 + P_d \tag{2.5}$$

$$v_u\{P_u + \rho_u(\frac{1}{2}v_u^2 + E_u)\} = v_d\{P_d + \rho_d(\frac{1}{2}v_d^2 + E_d)\} \tag{2.6}$$

where subscripts u and d denote upstream and downstream, respectively (see figure 2.1). Using the equation (2.4) and the equation of state for ideal gas, the equation (2.6) changes to

$$\frac{1}{2}v_u^2 + \frac{\gamma}{\gamma - 1}\frac{P_u}{\rho_u} = \frac{1}{2}v_d^2 + \frac{\gamma}{\gamma - 1}\frac{P_d}{\rho_d} \tag{2.7}$$

where γ is specific-heat ratio. From the equations of (2.4), (2.5), (2.7), and the equation of state for ideal gas, we obtain the equations of

$$\frac{\rho_d}{\rho_u} = \frac{v_u}{v_d} = \frac{(\gamma-1)P_u + (\gamma+1)P_d}{(\gamma+1)P_u + (\gamma-1)P_d} \tag{2.8}$$

$$\frac{T_u}{T_d} = \frac{P_u}{P_d} \cdot \frac{(\gamma-1)P_u + (\gamma+1)P_d}{(\gamma+1)P_u + (\gamma-1)P_d}. \tag{2.9}$$

The equations (2.8) and (2.9) are called Rankine-Hugoniot relations. The velocities are given as

$$v_u^2 = \frac{1}{2\rho_u}\{(\gamma-1)P_u + (\gamma+1)P_d\} \tag{2.10}$$

$$v_d^2 = \frac{1}{2\rho_u}\frac{\{(\gamma+1)P_u + (\gamma-1)P_d\}^2}{\{(\gamma-1)P_u + (\gamma+1)P_d\}} \tag{2.11}$$

In the case of $P_u \ll P_d$ (strong shock), we obtain

$$\frac{\rho_d}{\rho_u} = \frac{v_u}{v_d} = \frac{\gamma+1}{\gamma-1} \tag{2.12}$$

$$v_u = \sqrt{\frac{1}{2}(\gamma+1)\frac{P_d}{\rho_u}} \tag{2.13}$$

$$v_d = \sqrt{\frac{1}{2}\frac{(\gamma-1)^2 P_d}{(\gamma+1)\rho_u}} \tag{2.14}$$

v_u and v_d are defined in a coordinate where the shock front has null velocity. In the observer's coordinate, v_u equals the shock velocity ($\equiv v_s$) . Using the equation of state, the post-shock velocity $v_p \equiv v_u - v_d$, post-shock pressure $P_p \equiv P_d$, and the post-shock temperature $T_p \equiv T_d$ are obtained as

$$v_p = \frac{2v_s}{\gamma+1} \tag{2.15}$$

$$P_p = \frac{2\rho_u v_s^2}{\gamma+1} \tag{2.16}$$

$$kT_p = P_p\frac{\mu}{\rho_d} = \frac{2(\gamma-1)}{(\gamma+1)^2}\mu v_s^2 \tag{2.17}$$

where μ is the mean atomic weight, and k is the Boltzmann constant. In the case of $\gamma = \frac{5}{3}$, we obtain

$$kT_p = \frac{3}{16}\mu v_s^2. \tag{2.18}$$

$$\frac{\rho_d}{\rho_u} = \frac{v_u}{v_d} = 4 \tag{2.19}$$

The post-shock temperature is determined by the shock speed only.

2.1.3 Evolution of Supernova Remnant

After a supernova explosion, a large fraction of progenitor (mass= M_0) is ejected into the interstellar space with high velocity, which produces a shock wave. The evolution of SNR depends on the mass swept-up by the shock wave, the explosion energy, and the radiation energy. In this subsection, a brief summary of SNR evolution is presented.

Free Expansion Phase

The initial phase of the SNR evolution is called free expansion phase. In this phase, the mass within the shock front is dominated with the ejected matter (hereafter ejecta), which expands with little deceleration. Almost the all explosion energy is contained in the kinetic energy, while the thermal energy is small. The deceleration of the shock front starts when the swept-up mass becomes comparable with the ejecta mass, which is the end of the free expansion phase.

Adiabatic Phase

When the shock front is subject to a significant deceleration, the next phase of the SNR evolution called adiabatic phase starts.

In its early phase, the ejecta mass is not negligible compared with that of the swept-up matter. The ejecta heated by the shock wave makes an additional shock wave called reverse shock. The reverse shock propagates inward to the center of the SNR (opposite direction of the blast wave). The ejecta can be heated by the reverse shock, hence X-rays are radiated. Since both the ejecta mass and the density are larger than that of the swept-up matter, X-ray emission from the ejecta is dominant. X-ray spectroscopy in this stage provides key information for chemical composition of heavy elements synthesized by SN events.

When the swept-up mass becomes large, the ejecta mass is negligible compared with the total mass in the SNR. Sedov (1959) introduced a self similarity solution, which describes a evolution of SNRs in the adiabatic phase when the ejecta is negligible. Therefore, this stage is called the Sedov phase. In the polar coordinate, equation (2.1)–(2.3) are written as

$$\frac{\partial(v)}{\partial t}+\frac{\partial(\rho v^2+P)}{\partial r}=0 \tag{2.20}$$

$$\frac{\partial(\rho)}{\partial t}+\frac{1}{r^2}\frac{\partial}{\partial r}(r^2\rho v)=0 \tag{2.21}$$

$$\frac{\partial}{\partial t}(\frac{p}{\rho^\gamma})+v\frac{\partial}{\partial r}(\frac{p}{\rho^\gamma})=0 \tag{2.22}$$

where we assumed that the matter is ideal gas. Here we assume that an explosion with the energy of E_0 occurred in a uniform density of ρ_0. In SNRs, the pressure P_d is much higher than P_u, therefore we can neglect P_u compared with P_d. In that case, the dynamics of the SNR is determined by E_0 and ρ_0. Then, we can obtain a dimension-less parameter ($\equiv \xi$) consisting of r, t, E_0, ρ_0 as

$$\xi=(\frac{\rho_0}{E_0})^{1/5}\frac{r}{t^{2/5}} \tag{2.23}$$

Using the parameter of ξ, the shock radius R_s is given as

$$R_s(t)=\xi(\frac{E_0}{\rho_0})^{1/5}t^{2/5}. \tag{2.24}$$

In the case of $\gamma=\frac{5}{3}$, $\xi=1.15$. The equation (2.24) is converted to

$$R_s(t)=5.0(\frac{E_0}{10^{51}erg})^{1/5}(\frac{n_0}{1cm^{-3}})^{-1/5}(\frac{t}{10^3years})^{2/5} \qquad (pc) \tag{2.25}$$

$$v_s\equiv\frac{dR_s}{dt}=\frac{2}{5}\frac{R_s}{t} \tag{2.26}$$

Using the equation(2.18), the shock temperature (T_s) is given as

$$T_s = 5.2 \times 10^6 (\frac{E_0}{10^{51} erg})^{2/5} (\frac{n_0}{1 cm^{-3}})^{-2/5} (\frac{t}{10^3 years})^{-6/5}. \qquad (K) \qquad (2.27)$$

Using the equations (2.25), (2.27), (2.53), and an assumption of $T_s = T_e \equiv T$, we can estimate the age of SNR ($\equiv t_{age}$ years), n_0 (cm^{-3}), and the distance ($\equiv d$, pc) to be

$$\begin{aligned} t_{age} &= (\frac{E_0}{10^{51} erg})^{-1/5} (\frac{kT}{1 keV})^{-1/10} (\frac{r_s}{1'})^{-6/5} (\frac{F_X}{10^{-11} erg/sec/cm^2})^{3/5} \times 4.2 \times 10^3 & (2.28) \\ n_0 &= (\frac{E_0}{10^{51} erg})^{2/5} (\frac{kT}{1 keV})^{-4/5} (\frac{r_s}{1'})^{2/5} (\frac{F_X}{10^{-11} erg/sec/cm^2})^{-1/5} \times 0.74 & (2.29) \\ d &= (\frac{E_0}{10^{51} erg})^{2/5} (\frac{kT}{1 keV})^{-3/10} (\frac{r_s}{1'})^{-3/5} (\frac{F_X}{10^{-11} erg/sec/cm^2})^{-1/5} \times 3.2 \times 10^4 . & (2.30) \end{aligned}$$

X-ray flux of the free-free emission(F_X), angular radius (r_s) and temperature(kT) are observables. Thus assuming the explosion energy (E_0), we can solve the three equations (2.28)–(2.30), hence can estimate the three SNR parameters.

Cooling Phase

After the shock velocity is decelerated down to ~200 km/sec, the radiative cooling becomes significant (figure 2.2). This has a large impact on the dynamics of SNRs. The density behind the shock front is high, hence the time scale of the radiative cooling become small. Thus cool and dense shell is formed. In this phase, significant faction of the total energy has been already lost.

2.1.4 Plasma Condition

Since the plasma in SNRs are very tenuous, interactions among ions and electrons are very rare. Therefore it takes a long time for plasma to reach equilibrium. In this subsection, we will briefly review two types of non-equilibrium.

Non-equipartition of thermal energy between electrons and ions

Just after the shock, ions and electrons are heated up to high temperatures. Since the temperatures are proportional to the particle mass, proton temperature should be much higher than that of electron. Then electrons are gradually heated-up by the energy transfer from ions. The timescale of the energy transfer (τ_{ie}) is given by Spitzer (1962) as

$$\tau_{ie} = 9.9 \times 10^{12} \langle \frac{A_i}{Z_i^2} \rangle^2 \frac{(kT_e)^{3/2}}{n_e \ln \Lambda} \qquad \text{sec} \qquad (2.31)$$

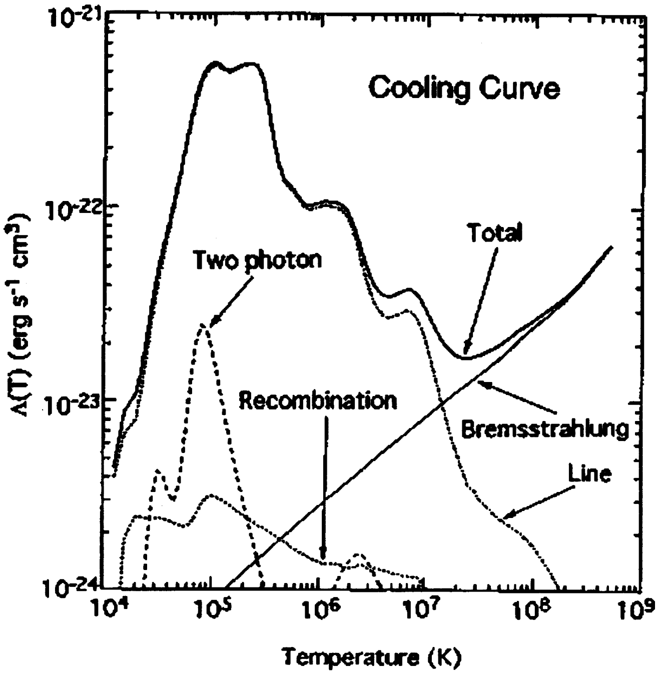

Figure 2.2: Cooling function adopted from Gehrels and Williams (1993).

where A_i, Z_i, kT_e, n_e, and Λ are ion mass in atomic units, ion charge, electron temperature in keV, electron number density in cm^{-3}, and the Coulomb logarithm, respectively. The large brackets in equation (2.31) means average value over various ions. With typical SNR values of A_i=1, Z_i=1, kT_e=1keV, n_e=1cm^{-3}, and Λ=30, the timescale of τ_{ie} is about 3×10^{11}sec$\simeq$ 10^4years, which is comparable or larger than the SNR ages. Therefore, electrons may not have the same energy as protons in young and/or low-density SNRs. This is called energy non-equipartition.

Non-Equilibrium Ionization

After the heat-up by the shock wave, the matter is ionized to some ionization degree depending on the electron temperature. Since the density and/or elapsed time after the shock-heating is small, the number of Coulomb collisions is also small. In this case, the ionization of matter may not reach to that expected from the electron temperature. This is called non-equilibrium ionization (NEI). After a long time, the NEI plasma may evolve to collisional ionized equilibrium (CIE) plasma, in which the ionization degree reaches to that determined by the temperature.

The characteristic timescale for plasma to reach CIE is given by Masai(1989) as

$$t_{ionize} \sim \frac{10^{12}}{n_e} \qquad \mathrm{sec} \tag{2.32}$$

where n_e is a electron density in cm^{-3} In an NEI state, more electrons are attached to ions compared with CIE. Since the photon energy and the intensity of line emissions depend on the ionization state (section2.4.2), we should be careful when we make plasma diagnoses.

2.2 Shell-like Supernova Remnants and Crab-like Pulsar

2.2.1 Shell-like SNR

In the adiabatic stage, almost the swept-up mass resides behind the shock front. The thickness of the swept-up mass ($\equiv r_t$) can be roughly estimated as following. The density of swept-up mass is $\sim 4n_0$ (equation(2.19)) in the downstream. Then we obtain an equation of

$$4\pi R_s^2 r_t \cdot 4n_0 = \frac{4}{3}\pi R_s^3 n_0 \tag{2.33}$$

where R_s is the shock radius. This equation gives

$$r_t = \frac{1}{12} R_s. \tag{2.34}$$

We can see that the swept-up matter resides in a thin shell. Therefore the SNRs in the adiabatic phase can be observed with the shell-like morphology in the X-ray band (figure 2.3). Using the equation (2.53), the luminosity of free-free emission (section 2.4.1) from the shell region is given as

$$L_x = 4\pi R_s^2 \cdot \frac{1}{12} R_s \cdot (4n_o)^2 \Lambda_{ff}(T) = \frac{16}{3} R_s^3 n_0^2 \Lambda_{ff}(T) \tag{2.35}$$

In the radio band, many SNRs are observed with the shell-like morphology, while the radio emission is thought to be non-thermal in origin (section 2.3.4), which is in contrast with the X-ray band.

2.2.2 Crab-like pulsar

Type-II SNe leave neutron stars (or black holes) after the explosion (section 2.1.1). When the neutron star spins rapidly and contains strong magnetic field, it can emit pulsating radio - X, and gamma-rays, which is called a pulsar. A pulsar often accompanies nebulosity with a center filled morphology. In the X-ray band, pulsars and nebulae are observed as non-thermal emission; pulsars exhibit coherent pulsation with period shorter than 1 seconds. Therefore, it can be distinguished from the shell-like SNRs.

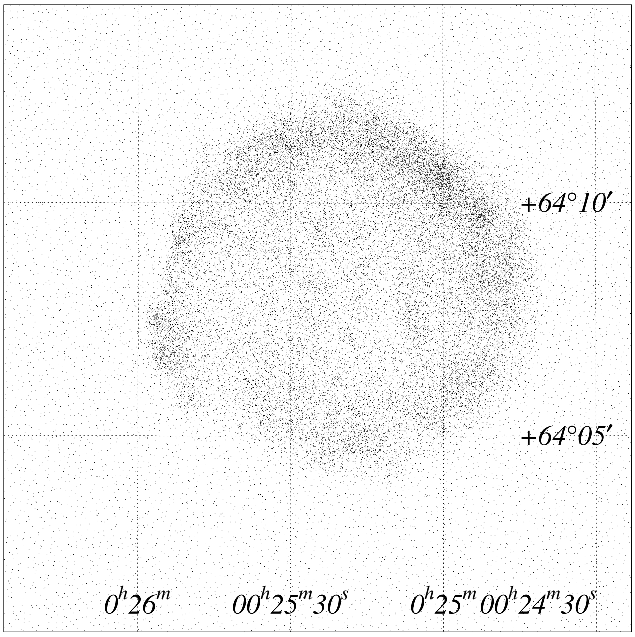

Figure 2.3: The *ROSAT*/HRI image of Tycho SNR as an example of shell-like SNRs. The image was taken from `http://legacy.gsfc.nasa.gov/cgi-bin/W3Brouse/` .

2.3 Cosmic Ray

2.3.1 Energy Spectrum

Figure 2.4 shows the energy spectrum of cosmic rays. As can be seen, the spectrum extends to $\sim 10^{20}$eV at least, which is much higher than the energy obtained with any particle accelerators in the world. The spectrum shown in figure 2.4 is expressed well with power-law functions as

$$N(E) \sim E^{-2.7} \qquad (<\sim 10^{15.5}\mathrm{eV}) \tag{2.36}$$

$$N(E) \sim E^{-3.0} \qquad (>\sim 10^{15.5}\mathrm{eV}) \tag{2.37}$$

In figure 2.4, we can see a power-law break at $\sim 10^{15.5}$eV, which is called 'knee'. Knee has been recognized as an important structure of the energy spectrum, since it can provide constraints on the acceleration mechanism and the source of cosmic rays. The energy density of cosmic rays is ~ 1 eV cm^{-3} (table 2.1). The energy densities of the starlight, galactic magnetic field, and the cosmic micro-wave background are ≤ 0.3 eV cm^{-3}, which are smaller than that of cosmic rays. Therefore cosmic rays form a major constituent of the interstellar medium.

	energy density(eV/cm^3)	note
cosmic rays	1.0	
magnetic field	0.3	$\sim 3\mu$G
radiation field	0.3	black body (2.7K)
optical light	<0.3	stellar light
turbulent flow	0.3	
thermal	0.01	neutral or ionized gas

Table 2.1: The energy densities of various items in the interstellar space. The values are adopted mainly from Hayashi and Hayakawa (1973).

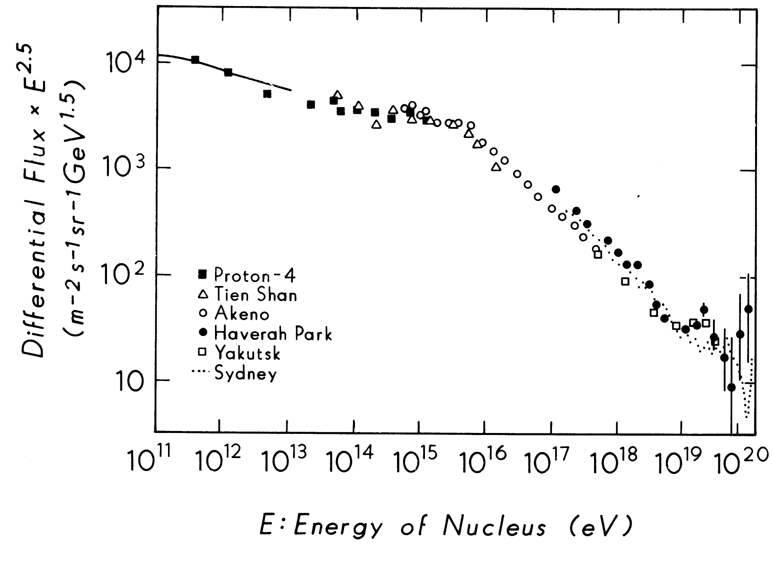

Figure 2.4: Energy spectrum of cosmic protons (Sokolsky 1989). The horizontal axis is energy (eV), and the vertical is (flux)×(energy)$^{2.5}$.

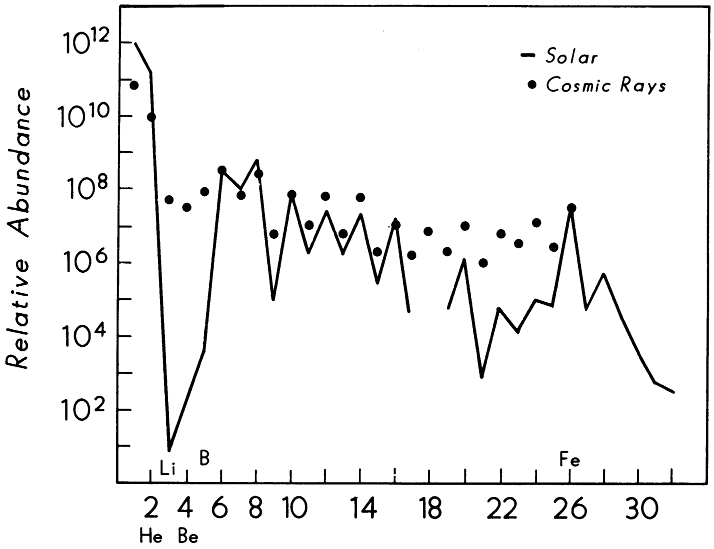

Figure 2.5: Chemical composition of cosmic rays (Sokolsky 1989). The horizontal axis is atomic number, and the vertical axis is relative abundance. The solid line indicates the solar abundance.

2.3.2 Chemical Composition

The chemical composition of cosmic rays is shown in figure 2.5. We can compare this average composition with the solar abundance (see figure 2.5). As can be seen, cosmic rays are significantly overabundant in Lithium, Beryllium, and Boron. Since these elements are not produced in the stellar evolution, they are thought to be produced by collisions of cosmic rays with the interstellar matter. Then, using the cross section of the spallation, the column density along the pass of cosmic rays from the birth place is estimated to be 5$\sim$10 g cm^{-2}. For a density of 1 proton cm^{-3}, the travel distance is estimated to be $\sim$1000 kpc, which is much larger than the diameter of the galaxy. Hence cosmic rays should be confined by the galactic magnetic field.

Electron is also a main composition of cosmic rays. Figure 2.6 is the energy spectrum of cosmic electrons (Tang 1984). Compared with that of protons, we can see that the electron spectrum becomes steeper at the higher energy, which is thought due to the synchrotron loss.

2.3.3 Energy Budget

We can estimate the energy injection rate into cosmic rays in the galaxy as follows (Gaisser 1990). From the observation of radioisotope such as ^{10}Be, the lifetime of cosmic rays ($\equiv t_{cr}$) is

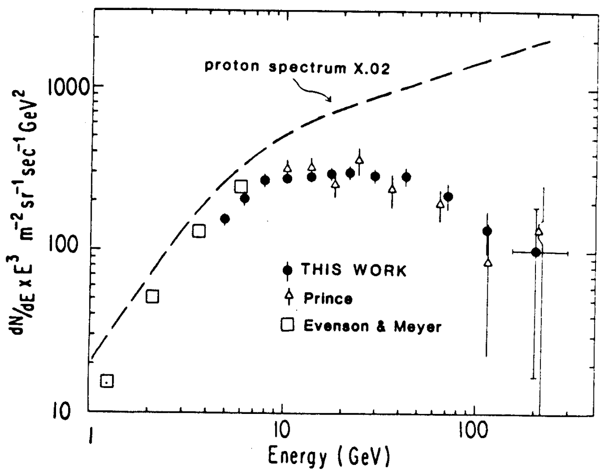

Figure 2.6: Energy spectrum of cosmic electrons from Tang (1984). Dashed line shows proton spectrum×0.02.

estimated to be

$$t_{cr} \sim 6 \times 10^6 \qquad \text{years.} \tag{2.38}$$

The lifetime is determined mainly by escape from the galaxy. The energy density of cosmic rays ($\equiv \epsilon_{cr}$) is given from table 2.1 as

$$\epsilon_{cr} \sim 1 \ \text{eV cm}^{-3} \tag{2.39}$$

The volume of our galaxy (V_G) is given as

$$V_G \simeq \pi \times r_g^2 \times d_g \sim \pi \times (15kpc)^2 \times 200pc \sim 4 \times 10^{66} \quad \text{cm}^3 \tag{2.40}$$

where r_g and d_g are the radius and the thickness of the disk of the galaxy, respectively. Using these values, the energy-injection rate into cosmic rays is roughly estimated to be

$$L_{cr} = \frac{V_G \cdot \epsilon}{t_{cr}} \sim 5 \times 10^{40} \, \text{ergs sec}^{-1}. \tag{2.41}$$

It is difficult to supply this huge energy by any of the astrophysical object except a few such as SNRs. SN events are estimated to occur in the galaxy at a rate of $R_{SN} \sim 30$ year^{-1} $\sim 10^{-9}$ sec^{-1}, with a typical kinetic energy of $E_{SN} \sim 10^{51}$ ergs/SN (section 2.1.1). Therefore, if 5% ($= L_{cr}/(E_{SN} \cdot R_{SN})$) of the kinetic energy is transfered from SNRs to cosmic rays, the energy budget problem may be resolved.

2.3.4 Acceleration of Cosmic Rays

Fermi Acceleration

Although SNRs have been thought as the possible source of cosmic ray energy, the acceleration mechanism had been unclear. It is about 20 years ago that the idea of the (first order) Fermi acceleration in the SNR shock front appeared (Bell 1978, Blandford and Ostriker 1978). The Fermi mechanism is the generally accepted model for the cosmic-ray acceleration. Suppose that there are two moving medium whose velocities are v_d and v_u ($v_u > v_d$, figure 2.7). This situation is realized in the shock front of SNRs. A particle scattered back elastically in the downstream changes its energy from E_0 into E_0' as

$$E_0' \simeq \gamma_d^2 (1 - \beta_d)^2 E_0 \tag{2.42}$$

where $\gamma_d \equiv \sqrt{1 - \beta_d^2}$ and $\beta_d \equiv \frac{v_d}{c}$. c is the light speed. Conversely, the particle energy changes in the upstream by a scattering as

$$E_1 \simeq \gamma_u^2 (1 + \beta_u)^2 E_0' \simeq (1 - 2\beta_d)(1 + 2\beta_u) E_0 \tag{2.43}$$

where we assume $\gamma_u \simeq 1$, $\gamma_d \simeq 1$, and $\beta_d \ll 1$, $\beta_u \ll 1$, which indicates that the shock speed is non-relativistic. Since β_u is larger than β_d, particles obtain energy from the shock fluid during each round-trip between the two regions. The scattering occur through the interactions between charged particles and the magnetic field, not through Coulomb collisions. In the case of 3-dimension, particles are scattered in various direction, therefore equation (2.43) is somewhat modified. The mean particle energy after n round trips is given as (Bell 1978),

$$E_n = E_0 \cdot exp\left(\frac{4}{3} n (\beta_u - \beta_d)\right) \tag{2.44}$$

Bell (1978) calculated the probability($\equiv \eta_s$) that the scattered particles escape from the acceleration region for each round trip as

$$\eta_s = 4 \frac{v_d}{v_p} \tag{2.45}$$

where v_p is a particle velocity. Hence the probability that a particle makes n round trips is given as

$$P_n = (1 - \eta_s)^n = (1 - 4\beta_d)^n \tag{2.46}$$

where we assumed $v_p = c$ (particle is relativistic). Using the equation of (2.46), we can calculate the differential energy spectrum of accelerated particles as

$$N(E) \propto \frac{dP_n}{dE_n} \propto E^{-\frac{\beta_u + 2\beta_d}{\beta_u - \beta_d}}. \tag{2.47}$$

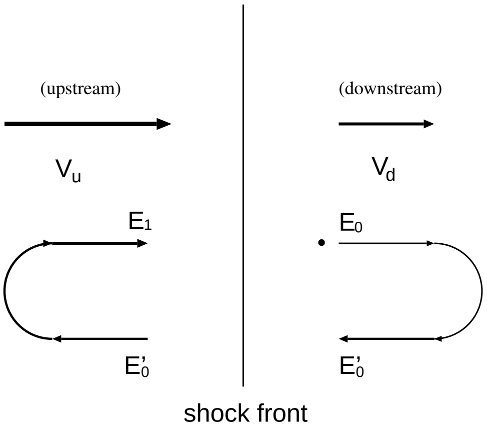

Figure 2.7: A schematic view of the Fermi acceleration.

In the case of $\beta_d = \frac{1}{4}\beta_u$ (equation (2.19)), we obatain an equation of

$$N(E) \propto E^{-2}. \tag{2.48}$$

Equation (2.48) is important from a point of view that the energy index is independent of the shock speed, but depends only on the ratio of the shock and pre-shock speeds.

Acceleration in Pulsar

Pulsars are also thought to be one of the acceleration sites for high energy cosmic rays. The energy source of the acceleration is the rotation power of the neutrons star. The rotation energy ($\equiv E_{NS}$) is given as

$$E_{NS} = \frac{1}{2} I \Omega^2 \tag{2.49}$$

where I and Ω are the moment of inertia and the angular velocity, respectively. For neutron stars with the mass = $1.4M_{\odot}$, radius = 10km, and $\Omega = 60\pi$ sec^{-1} (period = 33msec ~ Crab pulsar), we obtain $E_{NS} = 5\times10^{49}$ erg. In order to satisfy the energy budget of cosmic rays (L_{cr} :equation (2.41)), we need a Crab-like pulsar (E_{NS}) every 30 year in our galaxy.

2.3.5 Observational Evidence for Comic-Ray Acceleration in SNRs

While SNRs are candidates of cosmic-ray acceleration site, observational evidence has been poor. Although the radio emission from SNRs has been thought to be synchrotron from high energy electrons, the typical electron energies are ~10 GeV for a magnetic field of 10μG, which is much less than the knee energy. The recent X-ray and gamma-ray observations provided good

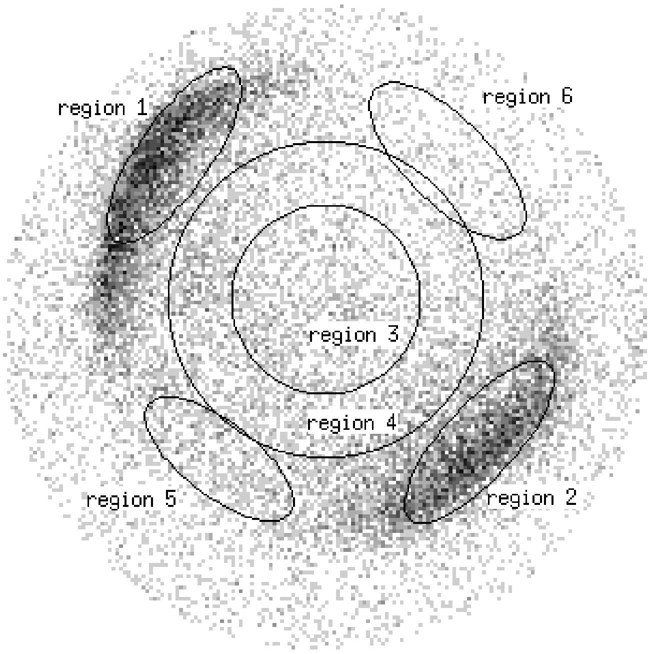

Figure 2.8: ASCA/GIS image of SN1006 (Ozaki 1997).

evidence for high-energy particles in SNRs. In this subsection, a brief summary of observations in various energy bands is presented.

X-ray —— ASCA

Koyama *et al* (1995) reported the result of ASCA observation of SN1006. Figure 2.8 is the X-ray image, and figure 2.9 is the X-ray spectra from the two bright shells and the center region. As can be seen, the X-ray spectrum from shell region includes no significant emission line, which suggests that X-rays have non-thermal origin. Koyama *et al* (1995) argued that the most plausible mechanism of non-thermal X-rays is synchrotron emission (section 2.4.3) from high energy electrons. For a magnetic field of $\sim 10\mu$G, the electron energy is estimated to be $\sim$100TeV (equation (2.58)), which is close to the knee energy. The idea of the synchrotron emission is supported by fact that the non-thermal X-ray regions coincide very well with the radio bright shells. This can be taken as observational evidence of Fermi acceleration in SNRs.

MeV$\sim$GeV gamma-ray —— EGRET

Since MeV$\sim$GeV gamma-rays are produced via decay of π^0 particles, reaction products of high energy protons (cosmic rays) with the collision to interstellar matter, these gamma rays may

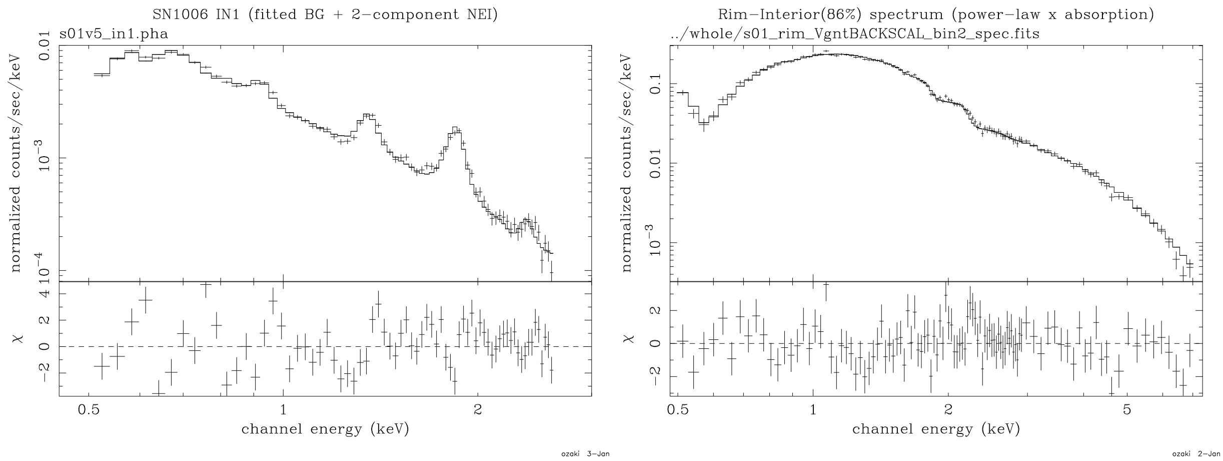

Figure 2.9: ASCA/SIS spectrum of SN1006 (Ozaki 1997). The left panel is the spectrum from the region3 of figure 2.8, and the right is from the region1 of figure 2.8.

indicate a site of the cosmic ray acceleration. Esposito *et al* (1996) investigated correlation between gamma-ray sources and radio bright SNRs using the data of the EGRET instrument onboard the Compton Gamma Ray Observatory (CGRO), and found that five SNRs spatially coincided with the EGRET sources. They estimated that the cosmic-ray densities in these SNRs were 100 times larger than that of the interstellar space, and proposed the SNRs to be cosmic-proton sources.

TeV gamma-ray —— CANGAROO

High energy electrons with energies about 100TeV can produce ~TeV gamma-rays through inverse Compton scattering (IC: section 2.4.4) of 2.7K cosmic-micro wave background. The ASCA discovery of high energy electrons in SN1006 drew much attention (Mastichiadis and Jager 1996) for a possibility to detect ~TeV gamma-rays.

The CANGAROO (the Collaboration between Australia and Nippon for a GAmma-Ray Observatory in the Outback) team searched for TeV gamma-rays from SN1006 with their air Čerenkov telescope and found significant excess of TeV gamma-rays (Tanimori *et al* 1998) from the non-thermal X-ray shell of the northeast rim. Since the gas density in this SNR is exceptionally small , the TeV gamma rays are not due to π^0 decay, but are most likely due to the IC process. Thus the discovery of TeV gamma-rays strongly supports the existence of ~100TeV electrons and the shock acceleration.

The TeV gamma-ray fluxes were estimated to be 4.6 ± 0.6(statistical)±1.4(systematic)$\times10^{-12}$

cm^2 sec^{-1}(>1.7±0.5TeV) and 2.4±0.5±0.7×10^{-12} cm^{2}sec^{-1} (>3.0±0.9TeV). Combined the IC model for the TeV gamma with the synchrotron radiation for the ASCA non-thermal X-rays, a magnetic field is uniquely determined to be 6.5μG.

2.4 X-ray Emission from Supernova Remnants

In this section, we review the X-ray emission mechanisms of bremsstrahlung, synchrotron, inverse Compton, and the line emission. The equations in this section are mainly adopted from Rybucki and Lightman (1979).

2.4.1 Bremsstrahlung (Free–Free Emission)

Radiation due to the acceleration of charged particles in the Coulomb field of other charged particles is called bremsstrahlung or free-free emission. The most realistic case of the bremsstrahlung is that electrons are accelerated by the Coulomb field of ions. The emission power of the bremsstrahlung per unit time and volume, and unit frequency is given by

$$\frac{dW}{d\nu dVdt} = \frac{32\pi^2 e^6}{3\sqrt{3}c^3 m^2 v} n_e n_i Z^2 g_{ff}(v,\nu) \tag{2.50}$$

where $g_{ff}, n_e, n_i, e, m, v, c, Z$ are Gaunt factor, electron density, ion density, charge unit, electron mass, electron velocity, light speed, and charge number of ion, respectively. In the case that electrons have velocities determined by a thermal distribution, the free-free emission is called thermal bremsstrahlung. The emission power of the thermal bremsstrahlung is given as

$$\frac{dW}{d\nu dVdt} = \frac{2^5\pi e^6}{3mc^3}(\frac{2\pi}{3km})^{1/2} n_e n_i T_e^{-1/2} Z^2 e^{-h\nu/kT_e} \bar{g}_{ff} \tag{2.51}$$

where $\bar{g}_{ff}$ and k are the velocity averaged gaunt factor and Boltzmann constant, respectively. In CGS units, equation (2.51) becomes

$$\frac{dW}{d\nu dVdt} = 6.8 \times 10^{-38} Z^2 n_e n_i T_e^{-1/2} e^{-h\nu/kT_e} \bar{g}_{ff} \quad (\mathrm{erg\ sec^{-1}\ cm^3\ Hz^{-1}}). \tag{2.52}$$

$\bar{g}_{ff}$ is a value with order of unity. In this thesis, we define as

$$\Lambda_{ff}(T_e) \equiv \int \frac{dW}{d\nu dVdt} d\nu. \tag{2.53}$$

2.4.2 Line Emission (Bound-Bound Emission)

The transitions between two discrete quantum levels often accompany photon emission, which is called line emission or bound-bound emission. In the simplest case of hydrogen, the photon energy in the transition between n' and n ($n' > n$, n and n' are the principal quantum numbers) is given as

$$E_{bb} = Ry(\frac{1}{n^2} - \frac{1}{n'^2}) \tag{2.54}$$

where Ry is Rydberg constant (= 13.6 eV). For heavy elements, equation (2.54) roughly becomes

$$E_{bb} = Z^2 Ry(\frac{1}{n^2} - \frac{1}{n'^2}). \tag{2.55}$$

In reality, the line energy of E_{bb} depends on the ionization states, azimuthal quantum number, and so on. For example, hydrogen-like atoms (only one electron is attached to ion) emit photons with the energy higher than that of He-like ones (ions with two electrons). For heavy elements, photon energies due to the transition between n'=2 and n=1 fall into the X-ray band. Thus high temperature plasma emit strong X-ray emission lines from heavy elements. We, therefore, can do plasma diagnoses using the X-ray spectrum.

2.4.3 Synchrotron Emission

Charged particles accelerated by magnetic field are accompanied by electro-magnetic radiations. When the particles have relativistic velocity, the radiation is called synchrotron. The power of synchrotron emission from a single particle per unit frequency is given as

$$P(\omega) = \frac{\sqrt{3}q^3 B \sin(\alpha)}{2\pi mc^2} F(\frac{2mc\omega}{3qB\gamma_L^2 sin(\alpha)}) \tag{2.56}$$

where $B, \gamma_L, m, c, q, \alpha$ are the strength of magnetic field, Lorentz factor of relativistic particle, particle mass, light speed, particle charge, and the angle between particle momentum and magnetic field (hear after pitch angle), respectively. The function $F(x)$ is given as

$$F(x) = x \int_x^\infty K_{5/3}(\xi) d\xi \tag{2.57}$$

where $K_{5/3}$ is the modified Bessel function. Since the peak of $F(x)$ is at ~0.29 (figure 2.10), $P(\omega)$ has the emission peak at

$$\omega = 0.29 \frac{3qB}{2mc} \gamma_L^2 sin(\alpha) \tag{2.58}$$

For a relativistic electron of energy E_e, the peak energy of emitted photon (E_p) is given as

$$E_p \sim 200(\frac{B}{1\mu \mathrm{G}})(\frac{E_e}{100\mathrm{TeV}})^2 \sin(\alpha)\ \mathrm{eV} \tag{2.59}$$

By integrating equation (2.56), the total emission power is given as

$$P_{tot} = \frac{2q^4 B^2 \gamma_L^2 sin^2(\alpha)}{3m^2c^3} = \frac{2q^4 B^2 E_e^2 sin^2(\alpha)}{3m^4c^7}. \tag{2.60}$$

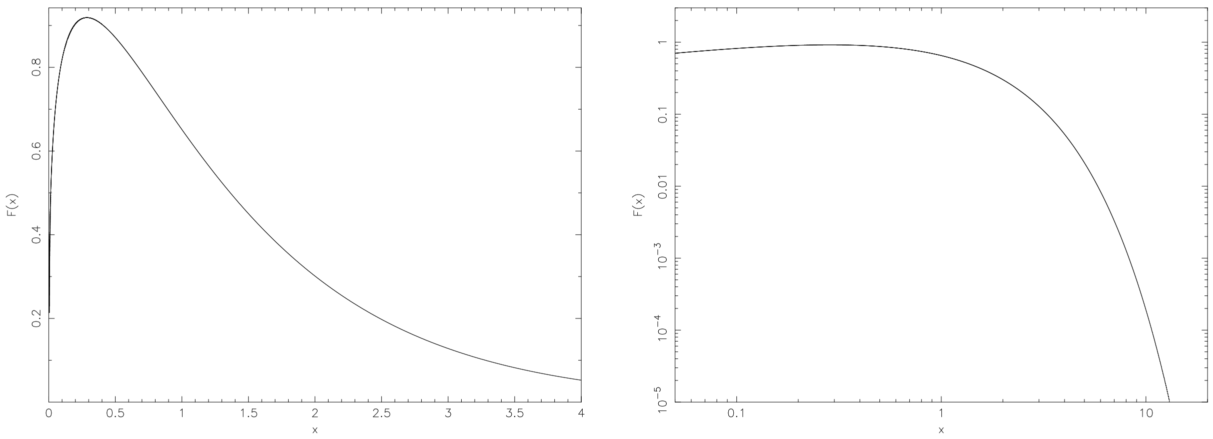

Figure 2.10: The profile of $F(x)$ (equation (2.57)). The left panel is drawn in a linear-linear scale, and the right is a log-log scale. The details of $F(x)$ are given in the text.

For relativistic electrons with the energy spectrum of a power-law as

$$N(E)dE = CE^{-p}dE \tag{2.61}$$

where C is constant, the emission power per unit frequency is given as

$$P_{pow}(\omega) = \frac{\sqrt{3}q^3CBsin(\alpha)}{2\pi mc^2(p+1)}\Gamma(\frac{p}{4}+\frac{19}{12})\Gamma(\frac{p}{4}-\frac{1}{12})(\frac{mc\omega}{3qBsin(\alpha)})^{-(p-1)/2} \tag{2.62}$$

In the case of Fermi acceleration which gives an energy index of electron to be $p \simeq 2$, the spectrum index of the synchrotron emission is 0.5 (photon index = 1.5). This value is almost the same as the canonical value of the non-thermal radio spectrum from SNRs, hence can be taken as evidence for the Fermi acceleration.

2.4.4 Inverse Compton

The scattering of high-energy photons by low-energy free electrons is called the Thomson scattering, in which photons partly lose their energies. Conversely, when the electron energy is sufficiently higher than that photons, the photon gains its energy from the electron. This process is called the inverse Compton scattering. The net power transfered from an electron to photons (radiation field) by the inverse Compton scattering is given as

$$P_{IC} = \frac{4}{3}\sigma_T c\gamma_L^2\beta^2U_{ph} \tag{2.63}$$

where σ_T, U_{ph}, and β are cross section of Thomson scattering, energy density of the radiation field, and the particle speed in a unit of c (light speed). For each photon, the energy change by a single collision averaged over the scattering angle is given as

$$E \simeq \gamma_L^2 E_0 \tag{2.64}$$

where E_0 and E are the photon energies before and after the scattering.

Chapter 3

Instruments

3.1 ASCA

ASCA (Advanced Satellite for Cosmology and Astrophysics, Tanaka *et al* 1994) is the 4th Japanese satellite for X-ray observation launched on 20 February 1993 by M-3SII-7 from Kagoshima Space Center. The satellite orbit just after the launch was semi-circular with a perigee of 522 km, apogee of 620 km, and an inclination of $31°$ with the orbit period of about 96 minutes. Figure 3.1 is a schematic view of ASCA in orbit. The weight and length are 417 kg and 4.7m long along the telescope axis, respectively.

ASCA has four observation instruments; two are Gas Imaging Spectrometer (GIS, Ohashi *et al* 1996) and the other two are Solid Imaging Spectrometer (SIS, Burke *et al* 1991), each placed at the focal plane of four identical X-Ray Telescopes (XRT, Serlemitsos *et al* 1995).

3.2 XRT

X-Ray Telescopes (XRT) were fabricated at National Aeronautics Space Administration (NASA) / Goddard Space Fright Center (GSFC), and calibrated at Institute of Space and Astronomical Science (ISAS). In orbit, the thermal shield is placed on the top of each mirror in order to minimize the mirror distortion by thermal stress.

The rough sketch of XRT is shown in figure 3.2. The incident X-rays are reflected twice by conical foils, and reach to the focal instruments. Since photons only with small incident-angle can be reflected by the foil, the X-ray effective area of each foil is small. Therefore the XRT has nest structure. Each XRT onboard ASCA consists of 120 layers of Al foils, still each XRT is made within the weight of 10 kg .

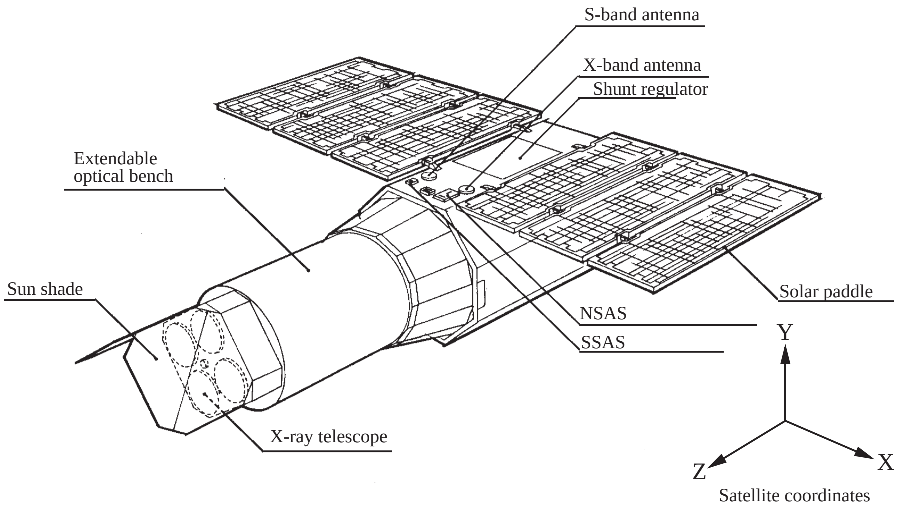
S-band antenna
X-band antenna
Shunt regulator
Extendable optical bench
Sun shade
Solar paddle
NSAS
SSAS
Y
X-ray telescope
Z
X
Satellite coordinates

Figure 3.1: schematic view of ASCA in orbit

The energy dependence of the effective area is shown in figure 3.3. The sudden drop near 2.2keV is due to the absorption edge of gold evaporated on the XRT foil. Since X-rays with the higher energy has the lower reflectivity, the effective area becomes smaller at the higher energy band. Figure 3.4 shows the off-angle dependence of the effective area.

Figure 3.5 shows point spread function (PSF) at several positions. The butterfly-like pattern is due to segmental structure of each mirror; one mirror consists of four identical quadrants.

Another problem on XRT is stray light: photons coming from outside of the field of view (FOV). Although the XRT geometry prevents such photons to reach the focal plane, the surface

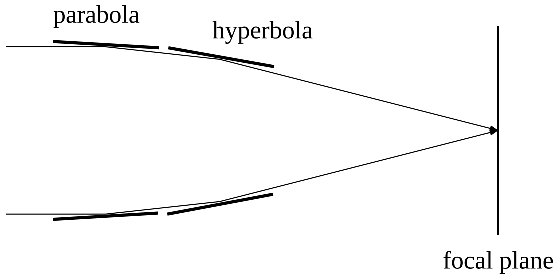
parabola
hyperbola
focal plane

Figure 3.2: rough sketch of XRT

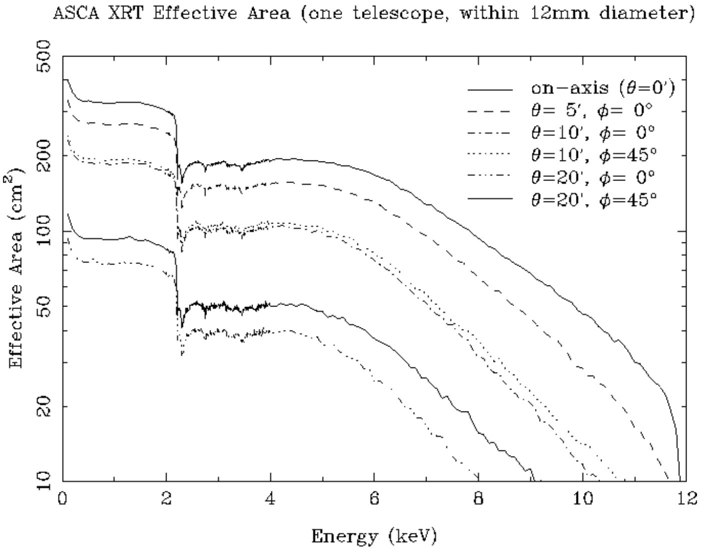

Figure 3.3: effective area of XRT. The horizontal axis is X-ray energy. The vertical axis is the effective area.

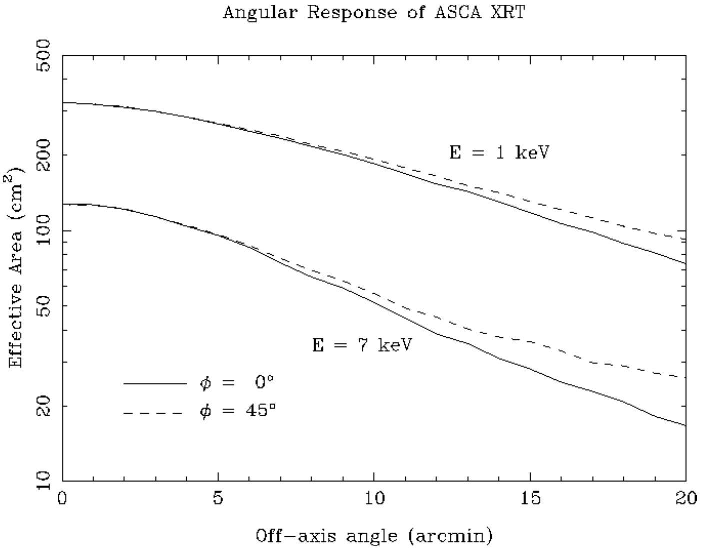

Figure 3.4: effective area of XRT. The horizontal axis is the distance from the on-axis point. The vertical axis is effective area. We show the data of 1.0 and 7.0 keV X-rays.

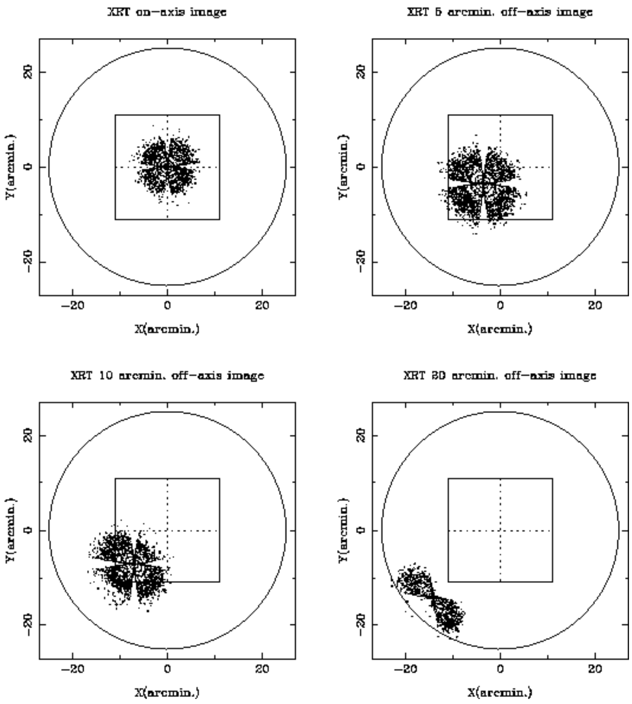

Figure 3.5: The point spread function of ASCA XRT.

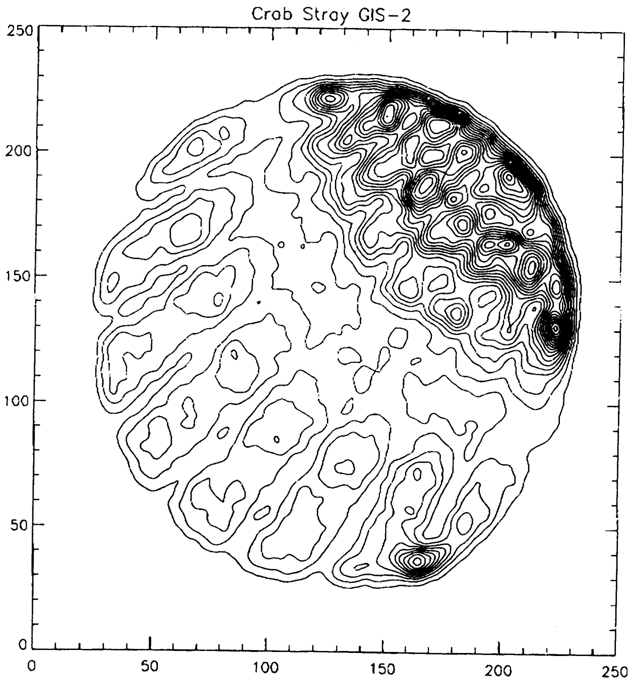

Figure 3.6: The stray light image obtained with GIS2. The Crab nebula is at the 1° from the detector center.

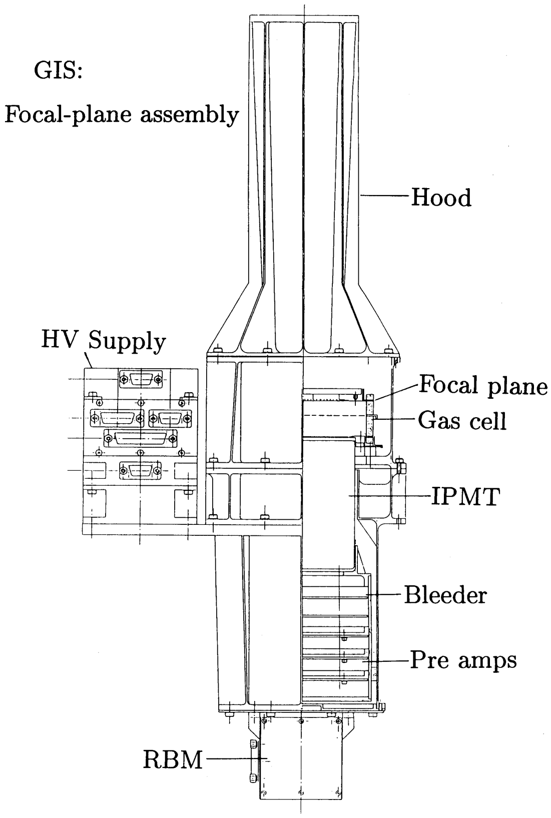

Figure 3.7: The cross section view of GIS. RBM is attached only to GIS-2

roughness, single or multiple reflections (more than two), or reflections at the back-side of conical foils make it possible. Figure 3.6 shows the GIS image of the stray light, in which the Crab nebula is located at 1° away from the detector center. Stray light becomes a serious problem when a very bright source is near the faint or extended sources.

3.3 GIS

3.3.1 Overview

GIS (Gas Imaging Spectrometer) was developed by Tokyo University, ISAS, and Tokyo Metropolitan University, with collaborators of Institute of Physical and Chemical researches (RIKEN), Kyoto University, GSFC, Meisei Electric Co. ltd, and Japan Radio Corporation Co. ltd (Ohashi *et al* 1996). ASCA has two GISs (GIS-2 and GIS-3) with a main electronics called GIS-E. The two detectors are identical except that GIS-2 has the radiation belt monitor (RBM). The concept and design of GIS are mainly based on gas scintillation proportional counter (GSPC)